GIANT H II REGIONS IN M81

MICHELE KAUFMAN[1,2]
Laboratory for Astronomy and Solar Physics, NASA Goddard Space Flight Center

FRANK N. BASH
University of Texas at Austin

R. C. KENNICUTT, JR.[3]
University of Minnesota

AND

P. W. HODGE[3]
University of Washington

ABSTRACT

Hα and VLA radio continuum observations at wavelengths of 6 and 20 cm are used to study the distribution of extinction and the distribution of giant radio H II regions along the spiral arms in M81. Radio flux densities, Hα fluxes, and extinction values are obtained for 42 giant H II regions with high surface brightness. The radial distribution of visual extinction A_v in the plane of M81 shows no trend, with an upper limit 0.1 mag kpc^{-1} for the radial extinction gradient and a mean A_v of 1.1 ± 0.4 mag.

Nearly all the giant radio H II regions lie along the spiral arms or the inner H I ring. The radial distribution of the set of giant radio H II regions exhibits a strong maximum at a galactocentric distance $R \approx 300''$ (4.7 kpc if the distance of M81 is 3.3 Mpc) and is more sharply peaked than the distributions of optical H II regions plotted by Connolly *et al.* and Hodge and Kennicutt, both of whom include faint H II regions as well as bright ones. Unless molecular hydrogen in M81 is also concentrated near $R \approx 300''$, our data disagree with Visser's model for star formation associated with a density wave. Some suggestions are made about how to change the ballistic particle model of Leisawitz and Bash to agree with the observed radial distribution of giant radio H II regions.

Subject headings: galaxies: individual (M81) — nebulae: H II regions — radio sources: galaxies

I. INTRODUCTION

The advent of the VLA,[4] recent developments in Hα image-tube technology, and the use of digitized images provide powerful new tools for research on H II regions in galaxies. This paper reports on the results of a high-resolution radio and optical study of giant H II regions in the relatively nearby Sab spiral M81. The specific purpose is to determine the spatial distribution of visual extinction in this galaxy and to trace the spatial distribution of recent star formation. The motivations for studying each of these problems will be discussed separately below.

To treat these two topics, we have taken VLA radio continuum data at wavelengths of 6 and 20 cm and measured absolute Hα fluxes for 42 giant H II regions in M81. From Bottinelli *et al.* (1984), we adopt a distance of 3.3 Mpc for M81. Then 10″ corresponds to 160 pc, which is a suitable linear resolution for detecting and measuring giant H II regions.

The distribution of extinction in M81 is of particular interest in view of Sarazin's (1976) results on the late-type spirals M101

and M33. From observations of the reddening and the radio-to-optical extinction of a small number of H II regions in M101 and M33, Sarazin finds evidence that internal absorption in the H II regions decreases as galactocentric distance R increases. Does a radial extinction trend occur in all types of spiral galaxies? In particular, does this phenomenon occur in an early-type spiral, such as M81, as well as in late-type spirals? Since a radial extinction gradient would affect the interpretation of broad-band colors along the spiral arms, it is important to know whether such a trend exists in M81.

From comparison of the radio flux densities and Hα fluxes, we determine the visual extinction A_v in the directions of the giant H II regions. While the term "giant H II region" is conventionally defined in terms of flux, the only H II regions that can be detected by the VLA at the distance of M81 are giant H II regions with high surface brightness. Because the radio data do not have high signal-to-noise (S/N) ratio, large H II regions (or collections of H II regions) with low surface brightness but large integrated flux are lost in the noise on the radio maps. We use the term "giant radio H II region" to refer to the subset of high surface-brightness regions detected in the radio. In M81, almost all of these regions are located on the spiral arms; therefore, our results pertain to extinction within the spiral arms. We take care to treat the radio and the Hα data in a consistent fashion so that the measured fluxes refer to the same region of space. Preliminary results based on 25 of these giant radio H II regions were reported by Kaufman, Kennicutt,

and Bash (1985). Since blue photographs of M81 reveal an intricate pattern of dust lanes (see Sandage 1961), we expect the extinction values for various H II regions to show some scatter. Therefore, it is important to measure a large number of H II regions, as we do here, before drawing conclusions about global trends.

The distribution of the giant radio H II regions in the plane of M81 is important for checking theories for star formation by a spiral density wave. Visser (1980a, b) presents detailed hydrodynamic calculations for a density wave in M81. Adopting a simple expression suggested by Shu (1974) for the star-formation rate, he predicts the radial distribution of star formation. Leisawitz and Bash (1982) use Visser's hydrodynamic model for the H I gas but have stars form in molecular clouds which they treat as ballistic particles. They predict the distribution of young stars and giant H II regions in the plane of M81. Both of these papers on M81 compare predicted star-formation rates with the global distribution of optical H II regions detected by Connolly, Mantarakis, and Thompson (1972; hereafter CMT) in M81 and adjust parameters to get a better fit to this observed distribution.

However, for testing these theories, the set of H II regions plotted by CMT has certain deficiencies. (1) CMT point out that their plate coverage is somewhat incomplete for $R = 4'.6–7'.2$ and seriously incomplete for $R > 7'.2$. In classical density wave models, the spiral arms extend from the inner Lindblad resonance to corotation, where the angular speed of the material equals the pattern speed. Since Visser places corotation at $R = 10'.7$, the incomplete plate coverage may cause some problems with interpretation of the radial distribution. (2) CMT do not distinguish bright H II regions from faint ones. But Mezger (1970) and Georgelin and Georgelin (1976) claim that giant H II regions are better tracers of spiral structure than less luminous H II regions are. Indeed, Rumstay and Kaufman (1983) find that in the late-type spirals M33 and M83 the distribution of high-luminosity H II regions is more concentrated in a two-armed pattern and more sharply peaked as a function of galactocentric radius than is the distribution of low-luminosity H II regions. They conclude that stochastic star formation is more important for producing the low-luminosity H II regions, whereas a spiral density wave is more relevant for star formation in giant H II regions.

Our $\lambda 20$ cm and Hα data provide better coverage of the M81 field than CMT have. All the H II regions that we detect in the radio are giant H II regions with high surface brightness. Therefore, the global distribution of giant radio H II regions presented here seems more appropriate for checking density wave theories in M81. We compare the observed radial distribution with the predictions of Visser (1980b) and Leisawitz and Bash (1982).

In §§ II, III, and IV we describe the observations and reductions and present a list of fluxes for the H II regions. We compare the radio and Hα luminosity functions of the set of giant radio H II regions. In § V we calculate the visual extinction from the Hα flux and the radio flux densities for each H II region. We show the radial distribution of extinction and compare the mean extinction values for the east and west arms. In § VI we show the distribution of giant radio H II regions in the plane of M81; this is compared with published distributions of optical H II regions that include faint regions as well as bright ones. We comment on how the radial distribution of giant radio H II regions compares with various theoretical predictions. We summarize our conclusions in § VII.

II. OBSERVATIONS

a) Hα

Calibrated Hα images of M81 were obtained in 1981 April, as part of a larger survey of star formation in nearby spirals by Kennicutt and Hodge. A two-stage Carnegie image-tube direct camera on the KPNO No. 1 0.92 m telescope was used to image a pair of 15' fields. When combined, these fields provide good coverage of M81. These fields will be referred to below as north Hα and south Hα. At each position, plates were obtained in Hα by using a 23 Å FWHM interference filter centered at 6560 Å, and in the red continuum by using a 100 Å filter centered at 6400 Å. Maps of relative surface brightness were generated by scanning the plates on the PDS digital microdensitometer at KPNO. Wedge sensitometer exposures obtained during the observing were used to calibrate the density-intensity relation of the plates. Digital maps of the surface brightness of the galaxy through the two bandpasses were then normalized so that the red continuum could later be subtracted from the raw Hα map to give the desired map of Hα intensity. Initial processing of the maps was performed at KPNO with the IPPS system, and final reductions were performed at the University of Minnesota Astronomical Image Processing Center with a local version of the NRAO AIPS program.

To calibrate the absolute flux scales on the Hα maps, photoelectric fluxes were measured for seven H II regions in M81 with the SIT vidicon cameras on the KPNO 2.1 m and the Palomar Observatory 1.5 m telescopes. The calibration procedures have been described elsewhere (Kennicutt 1981). Comparison of the nebular fluxes measured from the photographic and photoelectric data and comparison of the photoelectric flux values at the two observatories indicate that the fluxes of individual H II regions measured in this sample are accurate to $\pm 15\%$, while the overall flux scale should be accurate to $\pm 10\%$.

b) Radio Continuum

We have VLA data from B- and C-configurations at $\lambda 20$ cm and C- and D-configurations at $\lambda 6$ cm. The observations are described in more detail in Bash and Kaufman (1986). Table 1 lists the radio maps that we use here for studying the giant H II regions. The three maps are derived from a total of 43.5 hr of observations and have been interpolated to the same coordinate grid. The 20 cm map combines observations taken with B- and C-configurations, while the 6 cm map for the field M81 S combines observations taken with C- and D-configurations. These two maps form a "scaled-array" pair, i.e., each map samples approximately the same spatial frequencies as the

TABLE 1

RADIO CONTINUUM MAPS USED FOR MEASURING H II REGIONS IN M81

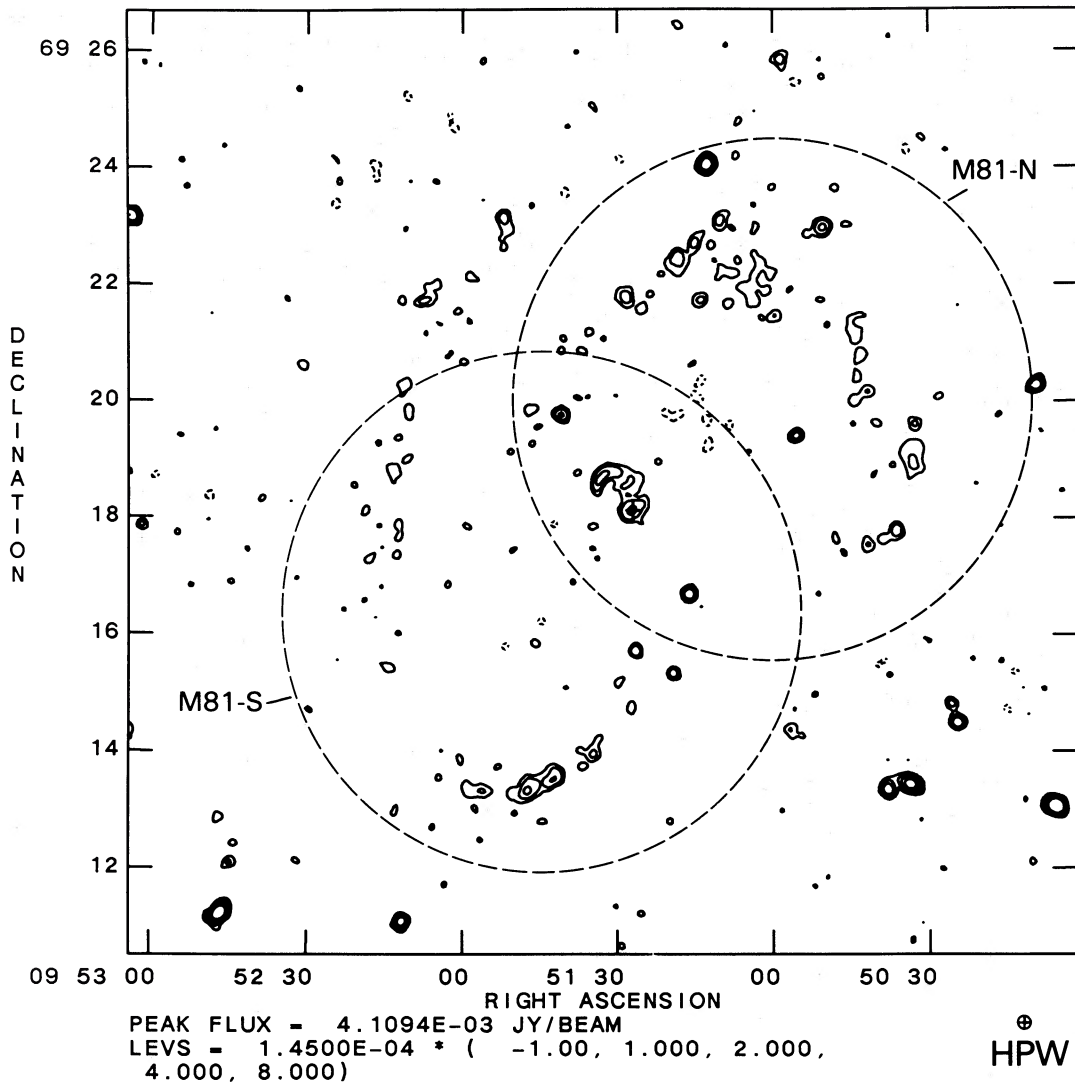| Parameter	Map 1	Map 2	Map 3
Field	M81	M81 S	M81 N
λ (cm)	20.5	6.1	6.1
ν (GHz)	1.465	4.885	4.885
VLA array	B, C	C, D	C
X_c	$0''.0$	$92''.0$	$-145''.0$
Y_c	$0''.0$	$-106''.2$	$111''.8$
Synthesized beam FWHM	$10'' \times 10''$	$10'' \times 10''$	$10'' \times 10''$
Cell	$1''.9 \times 1''.9$	$1''.9 \times 1''.9$	$1''.9 \times 1''.9$
Primary beam FWHM	$30'$	$9'$	$9'$
σ_{rms} (μJy/Ω_B)	48	25	47

FIG. 1.—A contour plot of the 20 cm continuum emission from M81 with the primary half-power beams for the two 6 cm fields marked by dashed circles. This display is not corrected for primary beam attenuation. The bright compact source in the nucleus was subtracted from the data at the location of the + sign. The solid contour levels are at 3 σ, 6 σ, 12 σ, and 24 σ, and the dashed contour level is at -3σ, where 3 σ equals 0.145 mJy/Ω_B.

other map. Table 1 gives the plane-of-sky displacement X_c, Y_c of the phase center of each map from the compact source in the nucleus of M81, with X positive to the east and Y positive to the north. The location of the compact source in the nucleus is $\alpha(1950) = 9^h51^m27^s340$, $\delta(1950) = 69°18'08''20$. The main body of M81, which extends about 20' along the major axis, is smaller than the primary half-power beamwidth at 20 cm but larger than the 9' primary half-power beamwidth at 6 cm. Two fields were mapped at 6 cm to provide 6 cm data on almost all of the H II regions detected in the 20 cm map. Figure 1 is a contour plot of the 20 cm map with the primary half-power beams for the two fields at 6 cm indicated. At 6 cm we measure the H II regions north of the minor axis of M81 on the map for the field M81 N (Map 3 in Table 1) and those south of the minor axis on the map for the field M81 S (Map 2 in Table 1).

For each map, Table 1 lists the value of the rms noise σ_{rms} before correction for primary beam attenuation. The noise is given in units of μJy/Ω_B, where Ω_B is the synthesized beam area of 113 arcsec². Before correction for primary beam attenuation, σ_{rms} is nearly uniform across the field of interest in each

map. We then corrected the maps for primary beam attenuation. This correction introduces a noise gradient which, at 6 cm, is significant within the field of interest. For example, within 1' of the phase center of M81 S the sensitivity at 6 cm is a factor of 1.9 better than at 20 cm, but 4'.5 away from the phase center of M81 S, the sensitivity is the same at both wavelengths. One needs to keep this variation in respective sensitivities in mind when comparing the list of H II regions detected at 6 cm with those detected at 20 cm.

From the 6 and 20 cm maps of Table 1, we compute values of the spectral index α (defined so that $S_\nu \sim \nu^\alpha$) for the various sources. Recall that $\alpha = -0.1$ for optically thin free-free emission. Bash and Kaufman (1986) measure eight sources in the overlap region of the two 6 cm fields and note the following calibration discrepancies: (a) the values of the flux density measured on the northern 6 cm map (Map 3) are 20% greater than those on the southern 6 cm map (Map 2); (b) for α close to -0.1, the average discrepancy in spectral index is

$$\alpha(N) - \alpha(S) = 0.14 \pm 0.04 , \qquad (1)$$

FIG. 3a

```
PEAK FLUX = 5.0741E+00
LEVS = 5.0000E-01 * ( 1.000, 1.500, 3.000,
     6.000, 12.00)
```

FIG. 3b

```
PEAK FLUX = 5.0741E+00
LEVS = 5.0000E-01 * ( 1.000, 1.500, 3.000,
     6.000, 12.00)
```
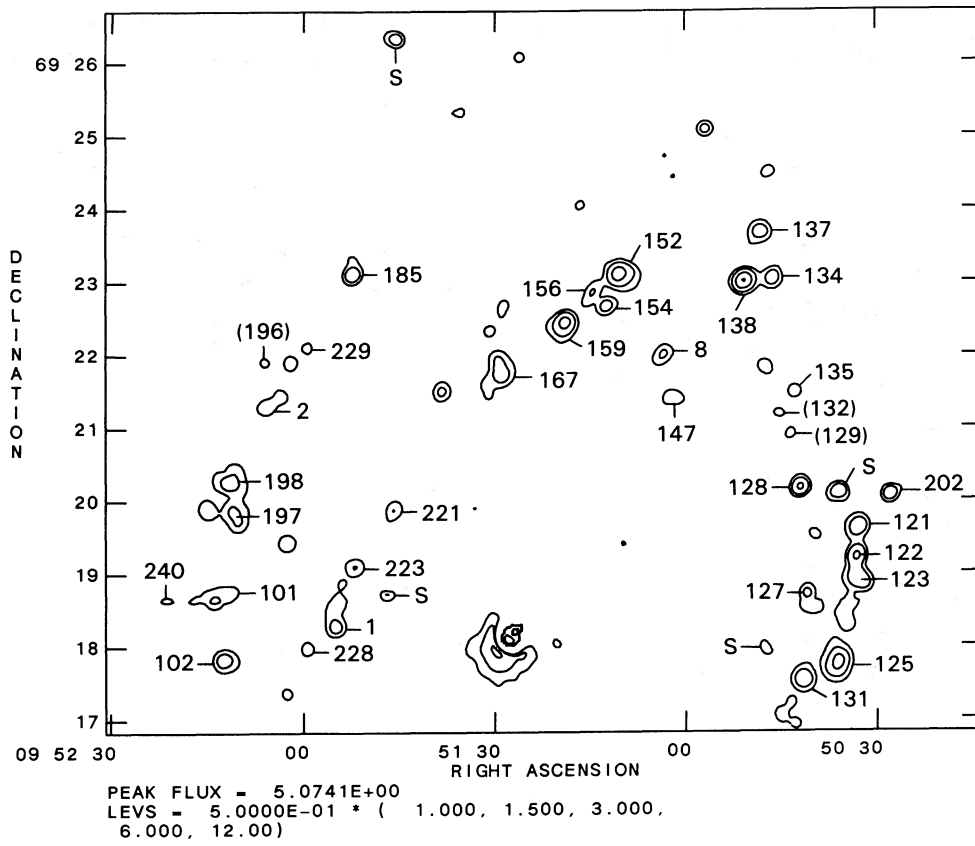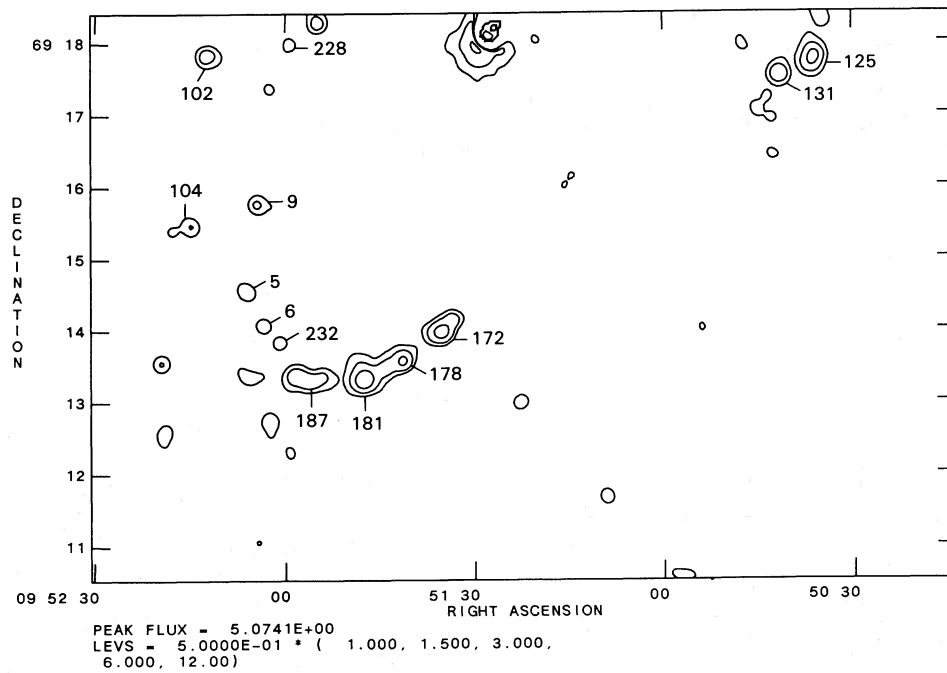
FIG. 3.—Contours plots of the spliced final Hα maps with the giant radio H II regions numbered. Stellar images are labeled with an S. Again the feature on the southeast side of the nucleus is an artifact.

where N and S refer to the northern and southern 6 cm maps, respectively.

c) Registration of the Hα and Radio Continuum Maps to the Same Coordinate Grid

For each digitized raw Hα map and red-continuum map, we did a plate solution with linear and quadratic terms and applied it to transform the maps into α, δ coordinates. The α, δ coordinates of 20 secondary standard stars were determined for us by Burton Jones on a 1979.09 epoch Lick astrographic plate, which contains SAO and AGK3 standards; positions for these stars will be provided upon request to the first author. We then interpolated the raw Hα and red-continuum maps to the same pixel size (1".9 × 1".9) and shifted to the same coordinate grid as the radio maps in Table 1. After this set of transformations, the standard deviations of the secondary standard stars are $\sigma(\alpha \cos \delta) = 0".5$, $\sigma(\delta) = 1".7$ for the north Hα map and $\sigma(\alpha \cos \delta) = 0".8$, $\sigma(\delta) = 0".6$ for the south Hα map, i.e., smaller than the pixel size. To determine the half-power width of the point-spread function on the Hα maps, we fitted stellar images with two-dimensional Gaussians. The red-continuum maps were then subtracted from the raw Hα maps and the resulting Hα intensity maps convolved to the same 10" × 10" resolution as the radio maps. These registered, convolved images will be called the final Hα maps.

III. H II REGIONS DETECTED AS RADIO SOURCES IN M81

Figure 2 (Plate 1) shows contours of 20 cm emission overlaid on a display of the final Hα maps with the north and south Hα images spliced together. A few stellar images did not subtract completely; these are labeled with an "S" in Figures 3a and 3b and include some stellar images that were blanked in the red-continuum map. Figure 2 shows the good correspondence between the brighter Hα sources and many of the 20 cm sources along the spiral arms. Table 2 lists the H II regions that we detect in the radio. To be included in this list (1) the peak intensity in the radio continuum must be at least 3 σ at either 20 cm or 6 cm and (2) if the source is below 3 σ at 6 cm (e.g., if the source is outside the 6 cm half-power beam), then there must be good correspondence in position between the Hα and 20 cm peaks. The list includes a few sources where the 6 and 20 cm flux values are consistent with optically thin free-free emission, but the Hα source is weak.

Table 2 gives the distance in the plane of the sky of each H II region from the nucleus, with X positive to the east and Y positive to the north. These coordinates refer to the approximate centroid of each H II region. To calculate the galactocentric distance R, we adopt an inclination of 59° and a position angle of 149° for the major axis, as in Visser (1980a). Correspondence between our H II regions and the H II regions in the catalog of Hodge and Kennicutt (HK) (1983a) is complicated by the fact that our maps are convolved to a much lower resolution. In column (10) of Table 2 we attempt to identify our sources with the HK regions. We have separated our listing according to whether the H II regions lie along the east arm, the west arm, or the faint inner H I ring discovered by Rots (1975). Bash and Kaufman (1986) note that the 20 cm arms appear to spiral outward from this ring (which has a radius of 4'.3 ± 0'.2 in a face-on image of M81).

The 42 Hα sources detected in the radio are numbered in the contour plots of the final Hα maps shown in Figures 3a and 3b. These regions have high surface brightness. Of the 33 H II regions with the highest peak Hα intensity, we detect 30 in the

radio, i.e., our radio maps detect 91% of the Hα sources with peak intensity $I(H\alpha) > 3.4 \times 10^{-14}$ ergs cm^{-2} s^{-1} pixel^{-1}.

Three sources labeled with numbers in parentheses in Figure 3a are dropped from consideration and not included in the tables because (1) the Hα source is embedded in extended 20 cm arm emission with the positions of the 20 cm and Hα peaks not in good correspondence and (2) no significant 6 cm flux is detected. These three sources may represent chance coincidences between structure in the nonthermal arm emission and Hα emission.

IV. Hα FLUX AND RADIO FLUX DENSITIES

a) Flux Measurement

We determine the radio and the Hα fluxes in a consistent fashion so that the ratio of radio-to-Hα flux is suitable for calculating the visual extinction A_v. For measuring the Hα flux $S(H\alpha)$, the 6 cm flux density $S_v(6)$, and the 20 cm flux density $S_v(20)$ of each giant radio H II region, we adopt a recipe similar to that developed by van der Hulst, Kennicutt, and Crane (1987) in their study of giant H II regions in M51 and NGC 6946.

The final Hα maps contain a positive background component that varies across the map and must be determined locally. In the radio maps, nonthermal arm emission may produce a local background. For each H II region, we integrate the source intensity over the same coordinates in the radio and the Hα maps and correct both the radio and the Hα data for local background in the same way. The choice of aperture size for the source and the measurement of the local background is complicated by noise in the radio data and structure in the nonthermal radio emission from the spiral arms. Because of S/N problems with the radio data, we do not attempt to include in the source aperture faint Hα emission that may be present in the outskirts of an H II region. The choice of source aperture for each H II region was determined by detailed inspection of the 6 cm, 20 cm, and Hα images and, where possible, was set by the 6 cm data to minimize the inclusion of nearby nonthermal radio emission. Except for four H II regions, the fluxes were measured by summing pixel intensities in a circular aperture, and the radius r_s of the source aperture was selected to be in the range $r_s = 7".6-13".3$ (120–210 pc). In the remaining four cases, we chose a rectangular aperture as a better fit to the distribution of free-free emission (see discussion of source 138 below). For the background aperture we used either a circular annulus around the source aperture or two circular apertures situated diametrically on either side of the source at a distance $2.5r_s$ from the source center. To calculate the net fluxes listed in columns (5), (7), and (9) of Table 2, we subtracted the median intensity in the background aperture from the source intensities. The uncertainties listed in columns (5) and (7) represent the noise errors in the net radio flux densities: $\sigma = \sigma_{rms}(A/\Omega_B)^{1/2}f_{PB}$, where A is the source area, Ω_B is the synthesized beam area, f_{PB} is the factor correcting for primary beam attenuation, and the values of σ_{rms} are listed in Table 1.

The Hα background corrections, which include instrumental and night sky contributions as well as diffuse Hα emission, range in value from 20% to 83%. Table 2 lists the values of the background corrections $B_c(6)$ and $B_c(20)$ to the 6 and 20 cm flux densities. These corrections were applied in all cases, even when the correction is less than the noise in the radio data. Compared to the noise in S_v, the background correction is
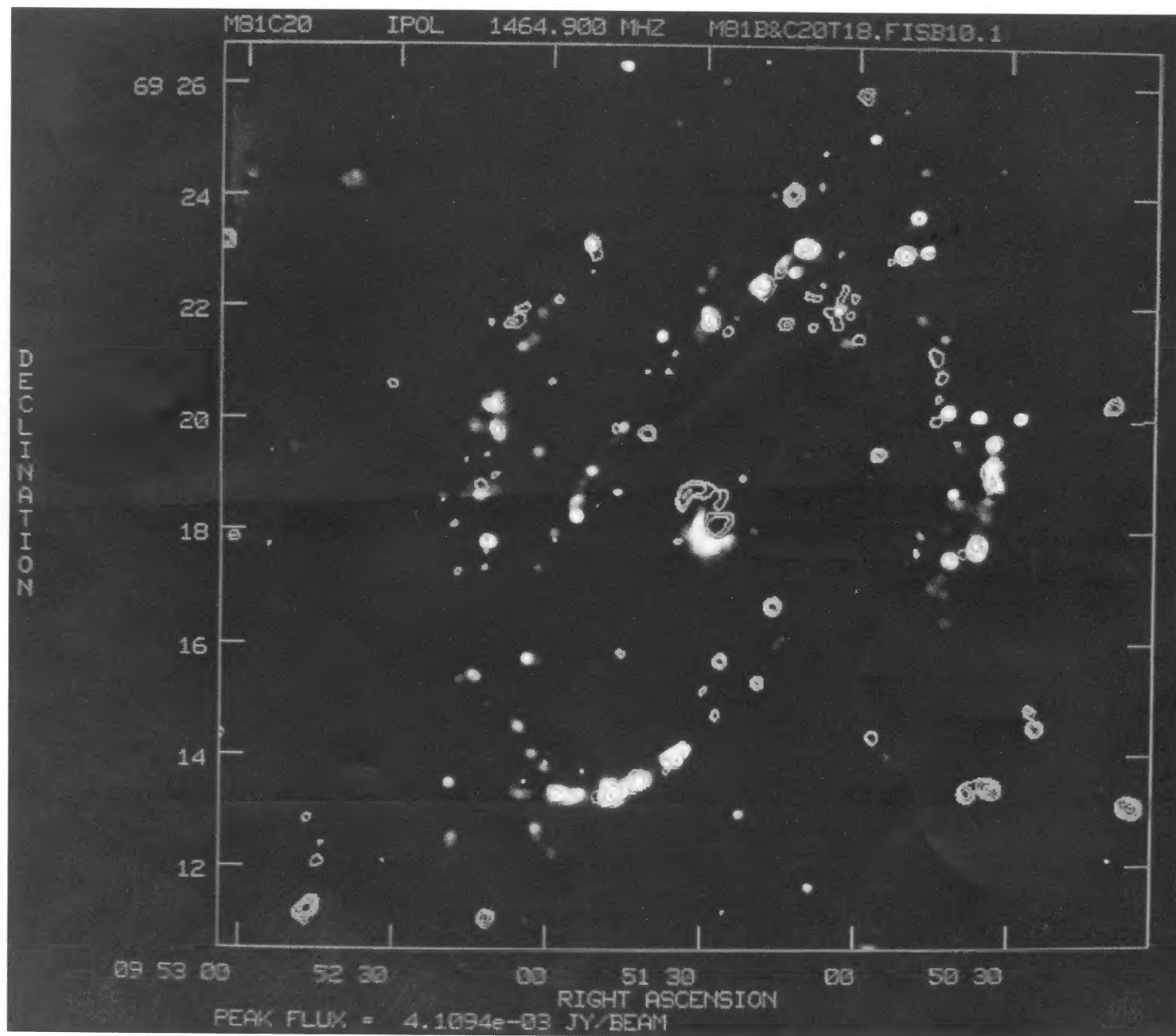
PLATE 1

FIG. 2.—The contour plot of 20 cm emission from Fig. 1 overlaid on a half-tone display of the final Hα maps to show the correspondence between Hα and radio continuum sources. The Hα feature on the southeast side of the nucleus is an artifact of incomplete subtraction of the red continuum light of the nuclear bulge.

KAUFMAN et al. (see page 65)

TABLE 2

GIANT RADIO H II REGIONS IN M81

Source (1)	X (2)	Y (3)	R (4)	$S_v(20)$[b] (5)	$B_c(20)$ (6)	$S_v(6)$ (7)	$B_c(6)$ (8)	$S(H\alpha)$ (9)	HK No. (10)
A. H II Regions Along the West Arm[a]									
8	−127	232	4.4	0.27 ± 0.10	0.34	0.22 ± 0.10	0.09	0.99	558
167	6	222	4.9	0.64 ± 0.09	0.17	0.54 ± 0.13	0.00	1.99	397
159	−48	253	5.0	0.74 ± 0.11	0.45	0.69 ± 0.13	0.08	2.93	453, 455, 458
154	−82	272	5.2	0.19 ± 0.08	0.09	≤0.097	...	1.17	489
156	−67	277	5.3	0.45 ± 0.08	0.11	0.50 ± 0.10	−0.17	1.01	467
152	−95	300	5.6	0.73 ± 0.11	0.13	0.80 ± 0.14	0.09	4.73	500
135	−234	201	5.8	0.18 ± 0.06	0.02	0.16 ± 0.07	−0.05	0.46	707
138	−196	293	5.9	0.70 ± 0.07	0.07	0.60 ± 0.09	0.02	3.43	652
128	−241	124	6.0	0.24 ± 0.08	0.18	0.29 ± 0.08	0.04	1.88	712
134	−219	296	6.2	0.11 ± 0.07	0.05	0.12 ± 0.08	0.06	0.77	692:
137	−207	333	6.5	0.27 ± 0.09	0.01	0.37 ± 0.12	−0.03	1.41	666, 672
127	−247	36	6.8	0.14 ± 0.06	0.02	≤0.066	...	0.70	719
131	−243	−36	7.5	0.26 ± 0.06	0.05	0.21 ± 0.08	0.02	1.58	714
121	−291	89	7.5	0.37 ± 0.08	0.05	0.40 ± 0.09	−0.03	1.81	767
122	−291	72	7.7	0.30 ± 0.08	0.11	0.39 ± 0.09	−0.02	1.80	763
123	−289	51	7.8	0.87 ± 0.11	0.28	0.87 ± 0.12	−0.05	3.96	761
202	−314	118	8.0	0.14 ± 0.07	0.04	0.17 ± 0.08	−0.01	1.12	785
125	−272	−21	8.1	0.80 ± 0.11	0.06	0.74 ± 0.14	0.09	4.79	744, 746
B. H II Regions Along the East Arm									
172	42	−245	4.8	0.57 ± 0.11	0.21	0.52 ± 0.07	0.11	4.90	343, 350
9[c]	199	−142	4.9	0.10 ± 0.06	−0.01	0.09 ± 0.03	0.01	0.62	152
173	49	−264	5.2	0.22 ± 0.07	0.03	0.22 ± 0.04	0.01	0.13	...
232	175	−257	5.2	0.23 ± 0.08	0.04	0.23 ± 0.05	0.01	0.30	...
178	80	−276	5.2	1.45 ± 0.11	0.05	1.01 ± 0.07	−0.02	3.96	305, 312
5	207	−215	5.3	0.13 ± 0.08	0.07	0.12 ± 0.05	−0.03	0.69	139
6	194	−243	5.3	0.11 ± 0.06	0.01	0.12 ± 0.04	−0.05	0.40	157
181	106	−285	5.4	1.59 ± 0.11	0.12	1.10 ± 0.07	0.03	6.82	268, 282
187	156	−287	5.5	0.63 ± 0.11	0.31	0.45 ± 0.08	0.00	3.51	214
104	253	−161	6.2	0.31 ± 0.08	0.03	0.16 ± 0.05	0.04	0.82	59, 68
102	238	−17	6.7	0.27 ± 0.08	0.06	0.27 ± 0.05	−0.01	1.27	80
101	243	36	7.5	0.61 ± 0.11	−0.03	0.20 ± 0.08	−0.03	1.19	84
197	228	101	8.1	0.25 ± 0.10	0.16	0.20 ± 0.09	0.02	1.26	108
240	281	27	8.5	0.17 ± 0.06	−0.01	0.09 ± 0.05	0.04	0.19	39
198	234	129	8.6	0.53 ± 0.10	−0.02	0.21 ± 0.10	−0.01	1.60	106
2	196	194	8.7	0.12 ± 0.10	0.23	...	...	0.50	155, 164
229	169	239	8.9	0.14 ± 0.06	0.06	...	...	0.25	206, 185
185	133	302	9.2	0.63 ± 0.08	−0.03	0.51 ± 0.22	0.10	1.60	241, 255
C. H II Regions Along the Inner H I Ring									
147	−133	198	4.0	0.18 ± 0.06	0.01	≤0.062	...	0.38	562
1	148	17	4.5	0.17 ± 0.11	−0.08	0.29 ± 0.06	0.03	2.01	230
221	103	101	4.6	0.24 ± 0.08	0.10	≤0.061	...	0.48	288
223	131	59	4.6	0.22 ± 0.08	−0.03	0.10 ± 0.05	−0.02	0.54	246, 253
230	188	−74	4.8	0.16 ± 0.06	0.01	0.11 ± 0.04	−0.02	0.15	165, 167
228	171	−11	4.8	0.19 ± 0.08	0.02	0.24 ± 0.05	−0.02	0.52	189

[a] X, Y in arcsec, R in arcmin, S_v and B_c in mJy, and $S(H\alpha)$ in units of 10^{-13} ergs cm^{-2} s^{-1}.

[b] S_v is the net flux density after subtraction of the background correction B_c.

[c] Source 9 lies between the east arm and the inner ring.

significant for $\frac{1}{3}$ of the cases at 20 cm and only 10% of the cases at 6 cm. Since the nonthermal radio arms in M81 are fainter than in M51, we expect that background corrections to the radio flux densities should be less significant for H II regions in M81 than in M51. Note that in some cases the background corrections to the radio flux densities are negative because of negative noise features or artifacts in the radio maps. (See Fomalont [1982] for a discussion of artifacts, both positive and negative, in VLA maps.)

Not all of the giant H II regions are detected at both 6 and 20 cm. We define the following detection classes: (1) detection class I represents the H II regions for which $S_v > 2\sigma$ at both 6 and 20 cm; (2) detection class II represents the H II regions for which $S_v > 2\sigma$ at only one radio wavelength. In almost all cases, the failure to detect the H II region at the second radio wavelength can be understood in terms of the uncertainties in the flux densities, since the ratio of 6 cm sensitivity to 20 cm sensitivity varies across the field. A few exceptions, where the values are consistent with nonthermal emission, are mentioned in § IVb when we discuss possible supernova remnants (SNRs). For sources not detected at 6 cm, $S_v(6)$ is omitted from Table 2 if the primary beam factor $f_{PB}(6) > 2.5$; otherwise $S_v(6)$ for undetected sources is given as a 1σ upper limit.

Table 3 lists the values of the excitation parameter where $U(20)$ is obtained from the net 20 cm flux density and $U(6)$ is obtained from the net 6 cm flux density. The 42 H II regions

TABLE 3

Values of Excitation Parameter,[a] Spectral Index, and Visual
Extinction for the Giant Radio H II Regions

Source (1)	$U(20)$ (pc cm^{-2}) (2)	$U(6)$ (pc cm^{-2}) (3)	α_c (4)	$A_v(20)$ (mag) (5)	$A_v(6)$ (mag) (6)
A. H II Regions Along the West Arm					
8.....	184	180	-0.15 ± 0.48	1.1 ± 0.5	1.0 ± 0.7
167.....	246	242	-0.15 ± 0.24	1.3 ± 0.3	1.2 ± 0.4
159.....	258	262	-0.06 ± 0.20	1.0 ± 0.3	1.0 ± 0.3
154.....	165	...	...	0.4 ± 0.6	...
156.....	218	236	0.09 ± 0.23	1.8 ± 0.3	2.1 ± 0.4
152.....	256	276	0.08 ± 0.20	0.3 ± 0.3	0.6 ± 0.3
135.....	161	(163)	(-0.08 ± 0.45)	1.6 ± 0.5	...
138.....	253	251	-0.12 ± 0.16	0.7 ± 0.3	0.7 ± 0.3
128.....	177	198	0.17 ± 0.36	0.0 ± 0.5	0.5 ± 0.4
134.....	135	147	0.10 ± 0.76	0.1 ± 0.9	0.5 ± 1.0
137.....	185	213	0.25 ± 0.38	0.6 ± 0.5	1.2 ± 0.5
127.....	148	...	...	0.7 ± 0.7	...
131.....	182	176	-0.19 ± 0.37	0.4 ± 0.4	0.2 ± 0.6
121.....	205	219	0.06 ± 0.26	0.7 ± 0.4	1.0 ± 0.4
122.....	192	217	0.20 ± 0.30	0.4 ± 0.4	0.9 ± 0.4
123.....	272	284	0.00 ± 0.16	0.8 ± 0.3	1.0 ± 0.3
202.....	148	165	0.16 ± 0.53	0.0 ± 0.7	0.4 ± 0.7
125.....	264	269	-0.06 ± 0.19	0.4 ± 0.3	0.5 ± 0.3
B. H II Regions Along the East Arm					
172.....	236	239	-0.08 ± 0.19	-0.1 ± 0.3	-0.1 ± 0.3
9.....	(132)	131	(-0.13 ± 0.62)	...	0.3 ± 0.6
173.....	171	180	0.03 ± 0.32	3.6 ± 0.5	3.8 ± 0.4
232.....	174	182	0.01 ± 0.36	2.5 ± 0.6	2.7 ± 0.4
178.....	323	299	-0.30 ± 0.09	1.5 ± 0.2	1.2 ± 0.2
5.....	143	(147)	(-0.04 ± 0.64)	0.5 ± 0.9	...
6.....	(136)	(147)	(0.09 ± 0.57)	...	...
181.....	333	307	-0.31 ± 0.08	0.9 ± 0.2	0.5 ± 0.2
187.....	244	228	-0.28 ± 0.21	0.5 ± 0.3	0.2 ± 0.3
104.....	192	162	-0.54 ± 0.35	1.5 ± 0.4	0.8 ± 0.5
102.....	185	192	-0.02 ± 0.29	0.8 ± 0.5	0.9 ± 0.3
101.....	241	173	-0.93 ± 0.38	2.0 ± 0.3	0.6 ± 0.6
197.....	180	173	-0.21 ± 0.48	0.7 ± 0.6	0.5 ± 0.6
240.....	156	132	-0.53 ± 0.59	2.7 ± 0.6	2.0 ± 0.9
198.....	230	177	-0.76 ± 0.41	1.3 ± 0.3	0.3 ± 0.7
2.....	140	...	...	0.9 ± 1.1	...
229.....	148	...	...	2.1 ± 0.7	...
185.....	244	237	-0.18 ± 0.38	1.6 ± 0.3	1.5 ± 0.6
C. H II Regions Along the Inner H I Ring					
147.....	159	...	...	1.8 ± 0.5	...
1.....	(159)	196	(0.41 ± 0.54)	...	0.4 ± 0.4
221.....	178	...	...	2.0 ± 0.5	...
223.....	172	(137)	(-0.66 ± 0.53)	1.7 ± 0.5	...
230.....	155	141	-0.35 ± 0.42	3.0 ± 0.6	2.6 ± 0.5
228.....	163	185	0.22 ± 0.39	1.5 ± 0.6	2.0 ± 0.3

[a] Values are listed in parentheses if the flux density before correction for background was less than 2 σ.

range in U from 130 to 330 pc cm^{-2} and thus qualify as giant H II regions according to the conventional definition. The value of U is listed in parentheses in Table 3 if the flux density before correction for background was less than 2 σ; for each of the latter sources, the spectral index α_c calculated from the net flux densities is consistent with -0.1 within the error bars. Nevertheless, in evaluating the visual extinction, we lump these sources with the detection class II sources.

b) Spectral Index Values and Possible SNRs

For each source, Table 3 gives the value of the spectral index α_c calculated from the net flux densities. In most cases, the background-corrected flux densities are dominated by optically thin free-free emission. Some of the exceptions can be attributed to either low S/N or insufficient background corrections, i.e., background corrections that did not completely remove adjacent nonthermal arm emission. However, a few of the exceptions may be supernova remnants. The following sources contain significant nonthermal contributions and may be considered as possible candidates for SNRs or SNRs embedded in OB associations: 101, 138, 147, 198, and 221. If Cas A were at the 3.3 Mpc distance of M81, then it would have a 20 cm flux density of 1.6 mJy; thus these sources have radio flux densities within the range expected for the most luminous

SNRs in M81. All these possible candidates for SNRs should be checked with spectrophotometry and velocity measurements.

Based on a preliminary analysis of their [S II]/Hα observations, J. Mazzarella and R. Kirschner (private communication) suggest that source number 138 may coincide with a possible SNR. In a spectral index map, we find that around the location of peak intensity there is a patch with an area of 126 arcsec^2 in which every one of 35 pixels has $\alpha = -0.1 \pm 0.2$. However, in the southeast part of the 20 cm and Hα emission region, the values of α become significantly nonthermal. While the size and location of the [S II] peak need to be checked, this source may be an OB association with an SNR on the southeast side. To measure the flux density of the H II region for Table 2, we used a rectangular aperture restricted to the region where α is close to -0.1. Since massive stars are thought to be the progenitors of Type II supernovae, we expect that some SNRs will be located in giant H II regions. In fact, Chu and Kennicutt (1986) find four examples of this in M101.

Garnett and Shields (1986) have done spectrophotometry of source 198 with a small ($4'' \times 4''$) aperture. They find that [S II]/Hα is somewhat higher than normal but not high enough to classify this source as an SNR. Source 198 may be another example in which an SNR is adjacent to an OB association. Long-slit spectroscopy would be helpful to check this suggestion.

The mean value of α_c for the entire set of sources in Table 3 is consistent with optically thin free-free emission, within the measurement uncertainty of ± 0.3. The flux density $S_\nu(6)$ was measured on the northern 6 cm map for all the H II regions on the west arm, and on the southern 6 cm map for almost all the

H II regions on the east arm. If we omit sources 101 and 198 for the reasons discussed above, then the discrepancy in the mean spectral index between H II regions on the west and east arms $\langle \alpha_c \rangle_{\rm west} - \langle \alpha_c \rangle_{\rm east} = 0.2$. This is less than the average measurement uncertainty and is consistent with the calibration discrepancy that Bash and Kaufman (1986) find between the northern and southern 6 cm maps (see eq. [1]).

Beck, Klein, and Krause (1985) have made low-resolution maps of M81 at wavelengths of 6.3 and 2.8 cm with the Effelsberg 100 m telescope. They note that the spectral index for the half of M81 southeast of the minor axis is significantly more nonthermal than for the northwest half. We computed the total flux from the giant radio H II regions northwest and southeast of the minor axis, respectively; the flux is 20%–40% greater in the northwest half. This is in the same sense as the spectral index asymmetry that they find, but the total 6 cm flux from our set of H II regions is too small to account, by itself, for the spectral index difference that they report.

c) Luminosity Function

Figure 4 shows the radio and Hα luminosity functions for the set of H II regions detected in the radio. Here $N_{\rm cum}$ is the cumulative number of H II regions with radio flux density greater than or equal to S_ν or Hα luminosity greater than or equal to $L(H\alpha)$, respectively. The plotted Hα values are not corrected for extinction; this explains the horizontal displacement of the Hα luminosity function from the 20 cm luminosity function. At 6 cm we do not have complete field coverage. Nevertheless, except at the low-flux end, all three luminosity functions have similar shape. If we restrict to values of $S_\nu(20) \geq 0.4$ mJy and $L(H\alpha) \geq 2 \times 10^{38}$ ergs s^{-1} (i.e.,
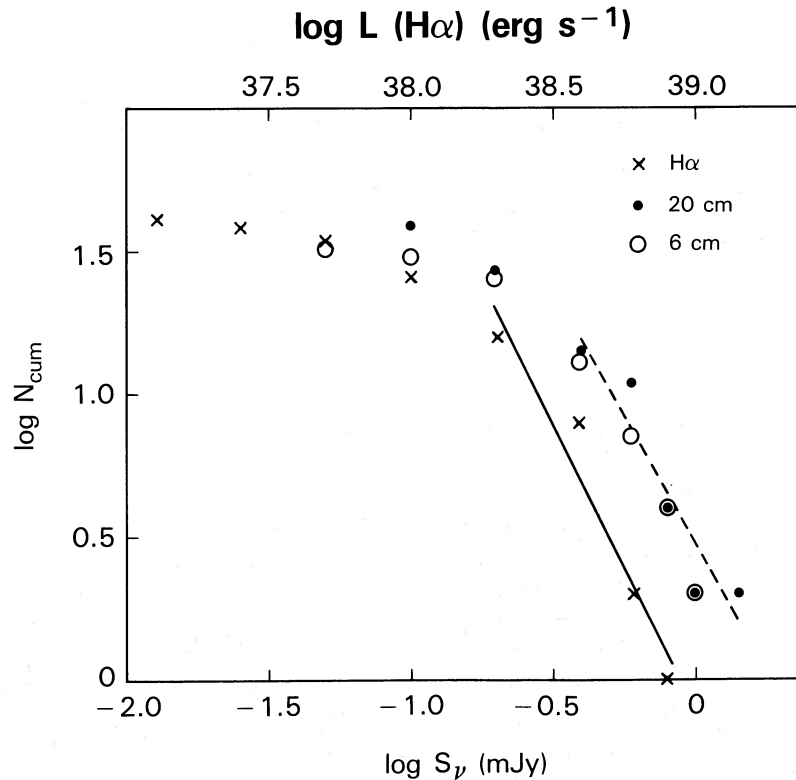

FIG. 4.—Radio and Hα luminosity functions for the giant radio H II regions. The straight lines represent power laws fitted to the data over the range indicated by the length of the line: the solid line pertains to the Hα data and the dashed line, to the 20 cm continuum data.

GIANT H II REGIONS IN M81

$S(H\alpha) \geq 1.6 \times 10^{-13}$ ergs s^{-1} cm^{-2}) to avoid any problems with incomplete sampling, then on fitting a power law of the form $N_{cum} \sim S_v^{-\beta}$, we obtain $\beta = 1.8 \pm 0.4$ for the 20 cm data and $\beta = 2.0 \pm 0.4$ for the Hα luminosity function. Our values of β lie within the range found for high-luminosity H II regions in some other galaxies. For the Hα luminosity function, $\beta = 2.2$ in M101 and NGC 5474 (Hodge 1986), $\beta = 1.65 \pm 0.15$ in the LMC and 1.75 ± 0.15 in the SMC (Kennicutt and Hodge 1986), $\beta = 1.5 \pm 0.2$ in NGC 628 (Kennicutt and Hodge 1980), $\beta = 1.4 \pm 0.2$ in M33 (Viallefond and Goss 1986), and $\beta = 1.4 \pm 0.2$ in M83 (Rumstay and Kaufman 1983). For the radio luminosity function, Viallefond and Goss (1986) obtain $\beta = 1.2 \pm 0.1$ in M33, and Israel (1980) finds $\beta = 1.2$ in the LMC.

V. VISUAL EXTINCTION

The extinction at Hα is

$$A_\alpha = 2.5 \log_{10} [C(v, T_e)S_v/S(H\alpha)] , \qquad (2)$$

where S_v is the optically thin free-free emission in the radio. We assume that the electron temperature T_e equals 10^4 K for the H II regions; then from Gebel (1968) one has $C(v, T_e) = 8.01 \times 10^{-13}$ ergs cm^{-2} s^{-1} mJy^{-1} if $v = 1.465$ HGz and $C(v, T_e) = 9.05 \times 10^{-13}$ ergs cm^{-2} s^{-1} mJy^{-1} if $v = 4.885$ GHz. To compute the values of the visual extinction A_v listed in columns (5) and (6) of Table 3, we adopt the standard galactic reddening law of Miller and Mathews (1972) and set $A_v = 1.28A_\alpha$. The values of $A_v(20)$ are calculated from $S(H\alpha)$ and $S_v(20)$, while the values of $A_v(6)$ are calculated from $S(H\alpha)$ and $S_v(6)$. If T_e were decreased from 10^4 K to 7000 K, then A_v would increase by 0.27 mag. The values listed for the uncertainty in A_v are based on a $\pm 15\%$ uncertainty in the Hα fluxes and the noise errors in the net radio flux densities. We present values for both $A_v(6)$ and $A_v(20)$ because our 6 cm maps do not provide complete coverage of M81 and the ratio of 6 cm to 20 cm sensitivity varies across the field of interest.

Figure 5a, b shows A_v plotted as a function of net radio flux density. Some large values of A_v occur among the weak sources (i.e., those with $S_v < 0.25$ mJy), but otherwise there is no particular trend.

a) Mean Values

Table 4 shows that the average visual extinction for giant radio H II regions in M81 is 1.1 ± 0.4 mag. If we restrict to the H II regions along the east and west arms, then $\langle A_v \rangle = 1.0 \pm 0.4$ mag. Since the mean value of α_c is consistent with free-free emission, the values of $\langle A_v(20) \rangle$ and $\langle A_v(6) \rangle$ agree within the measurement uncertainties. Including the sources in detection class II does not have a significant effect on the means. The uncertainties listed in columns (3) and (7) of Table 4 are derived from the error bars for the individual H II regions. Except for the inner ring, where the sample size n is small, these exceed the values for the dispersion listed in columns (4) and (8); thus, our error estimate for the mean visual extinction is dominated by the noise in the radio data. If we omit sources 101, 198, and 221 for the reasons discussed above, then the values of $\langle A_v(20) \rangle$ and $\langle A_v(6) \rangle$ for the east arm and for the inner ring change by less than or equal to 0.1 mag. Source 173 is apparently an H II region embedded in dust. Omitting it from the statistics decreases the mean A_v for the east arm by 0.2–0.3 mag and decreases the mean for the entire field by 0.1 mag. Within the errors bars $\langle A_v(6) \rangle$ is the same for the east arm as for the west arm. The discrepancy $\langle A_v(20) \rangle_{east} - \langle A_v(20) \rangle_{west}$ between east and west arms equals 0.7 ± 0.6 mag if source 173 is included and 0.5 ± 0.6 mag if source 173 is omitted. Thus we find that the mean extinction is roughly the same for the two arms. On the other hand, the mean extinction for the small sample of H II regions along the inner H I ring is greater than for the H II regions in the main arms. Since only two of the H II regions on the inner ring are detection class I sources, the best we can say is that our data give some indication of a higher extinction along the inner ring.

Is the extinction we measure largely internal to M81? From galaxy counts and H I column densities, Burstein and Heiles (1984) estimate that in the direction of M81 the foreground galactic blue extinction $A_B = 0.15$ mag [or $A_v = 0.1$ mag if $A_v/E(B-V) \approx 3$]. Peimbert and Torres-Peimbert (1981) and Bruzual, Peimbert, and Torres-Peimbert (1982) conclude that the reddening of the nucleus of M81 is $E(B-V) = 0.19$, and from the Balmer decrement suggest that about half of this is internal to M81. This would imply a foreground extinction

TABLE 4

AVERAGE VALUES OF VISUAL EXINCTION FOR GIANT RADIO H II REGIONS IN M81

| LOCATION (1)	DETECTION CLASS (2)	$\lambda = 20$ cm				$\lambda = 6$ cm			
		$\langle A_v(20) \rangle$ (m) (3)	s.e. (m) (4)	n (5)	Source omitted (6)	$\langle A_v(6) \rangle$ (m) (7)	s.e. (m) (8)	n (9)	Sources omitted (10)
West arm	I	0.7 ± 0.4	± 0.1	15	...	0.9 ± 0.4	± 0.1	15	...
West arm	I, II	0.7 ± 0.4	± 0.1	18	...	0.9 ± 0.4	± 0.1	15	...
East arm	I	1.5 ± 0.4	± 0.3	13	...	1.2 ± 0.4	± 0.3	13	...
East arm	I	1.4 ± 0.4	± 0.3	12	101	1.3 ± 0.4	± 0.4	11	101, 198
East arm	I	1.2 ± 0.4	± 0.2	11	101, 173	1.0 ± 0.4	± 0.3	10	101, 198, 173
East arm	I, II	1.4 ± 0.5	± 0.3	15	101	1.2 ± 0.4	± 0.4	12	101, 198
Inner ring	I	2.2 ± 0.6	± 0.8	2	...	2.3 ± 0.4	± 0.3	2	...
Inner ring	I, II	2.0 ± 0.6	± 0.3	5	...	1.7 ± 0.4	± 0.7	3	...
Inner ring	I, II	2.0 ± 0.6	± 0.3	4	221	1.7 ± 0.4	± 0.7	3	...
Entire field	I	1.1 ± 0.4	± 0.2	30	...	1.1 ± 0.4	± 0.2	30	...
Entire field	I	1.0 ± 0.4	± 0.1	28	101, 173	1.0 ± 0.4	± 0.1	27	101, 198, 173
Entire field	I, II	1.1 ± 0.5	± 0.2	37	101, 221	1.1 ± 0.4	± 0.2	30	101, 198
North half	I	0.9 ± 0.4	± 0.2	17	101	1.0 ± 0.5	± 0.1	16	101, 198
South half	I	1.2 ± 0.4	± 0.3	11	173	1.0 ± 0.4	± 0.3	11	173
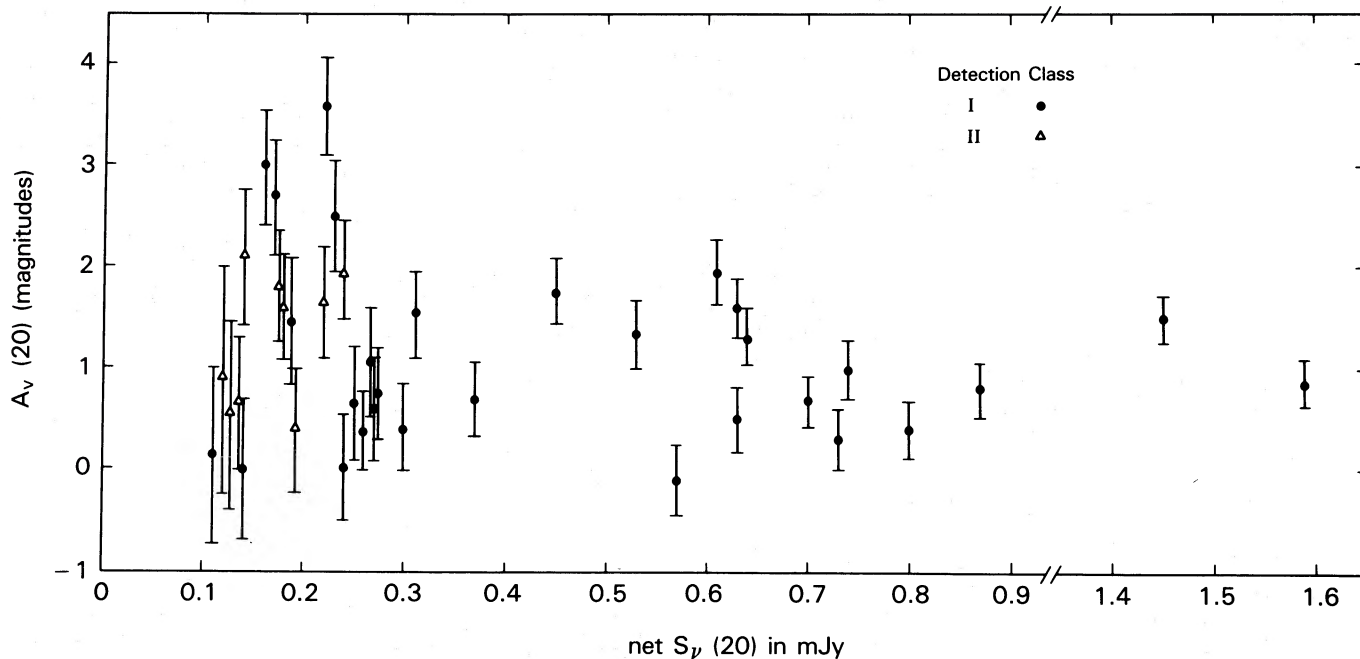
FIG. 5a
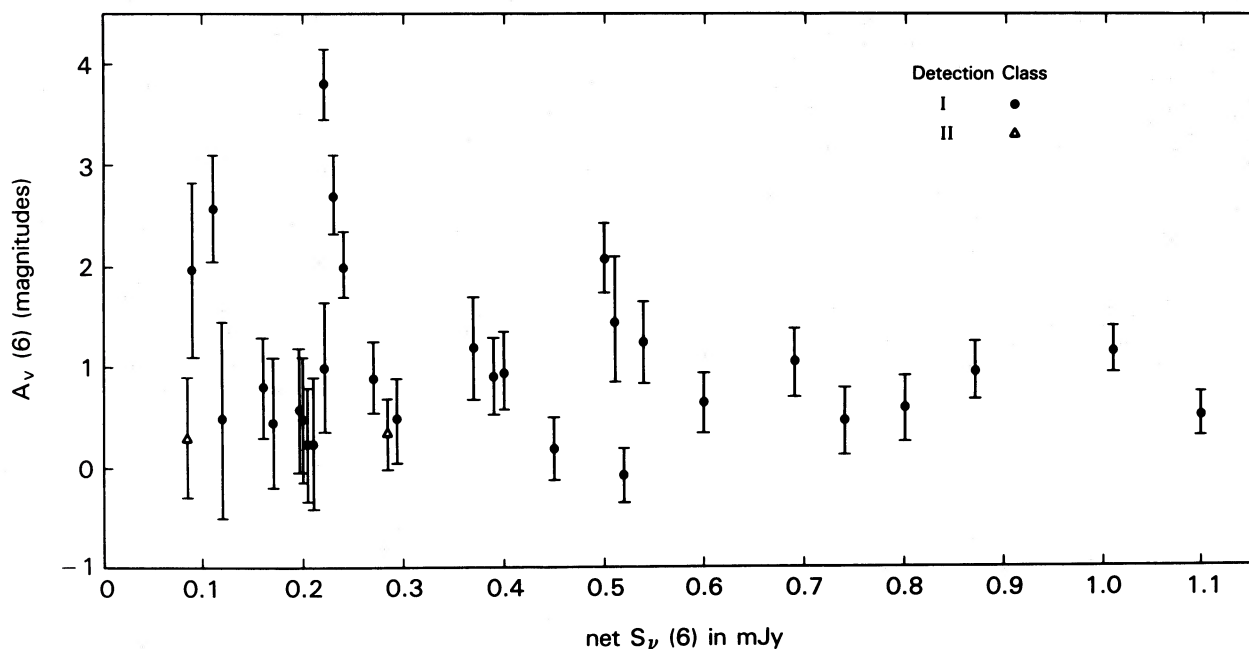
FIG. 5b

FIG. 5.—(a) Visual extinction $A_v(20)$ as a function of $S_v(20)$ for the giant radio H II regions. (b) $A_v(6)$ as a function of $S_v(6)$.

$A_v \approx 0.3$ mag. From his all-sky *IRAS* 100 μm map with zodiacal light subtracted, Boulanger (1986) finds that within $1°–1°5$ of the center of M81, the 100 μm intensity $I_v(100\ \mu m) = 4 \pm 1$ MJy sr^{-1}. He has obtained the following relation between the 100 μm intensity corrected for zodiacal light and A_v:

$$I_v(100\ \mu m) = (13\ \text{MJy sr}^{-1})\left(\frac{A_v}{1\ \text{mag}}\right). \qquad (3)$$

This implies that the foreground extinction near M81 is

0.3 $\pm$ 0.1 mag. All of these estimates are small compared to our mean value of A_v for the giant H II regions and indicate that most of the extinction we measure is internal to M81. One reservation is the following. Magnani and der Vries (1986) did star counts on a region a few degrees away from M81. Although they find an average A_v of 0.3 mag, their map shows patches as small as 8′ in which A_v reaches values as high as 0.8 mag.

The brightest 100 μm feature adjacent to M81 is the faint emission that Abolins and Rice (1986) identify with Arp's

Loop. This feature (see Arp 1965) surrounds roughly the northern half of M81 and appears to be connected with the straight dust lanes that cut across the northern part of the optical image. However, the Arp's Loop feature does not appear to contribute significantly to the visual extinction we detect in the directions of the giant H II regions. As is clear from Table 4, the mean extinction for the H II regions north of the nucleus is about the same as the mean extinction for the H II regions south of the nucleus.

We note that our mean value of 1.0 ± 0.4 mag for the visual extinction of the giant H II regions along the arms is not much greater than two other estimates of extinction in M81. From photometry in Johnson's J, H, and K bands, Humphreys et al. (1986) find $A_v = 0.8$–1.3 mag for the two brightest M supergiants in M81; one of these is on the west arm. Holmberg's (1958) statistical model predicts that an average early-type spiral with an inclination of $59°$ would have a mean internal A_v of 0.6 mag if the nuclear bulge is excluded. On the other hand, de Vaucouleurs, de Vaucouleurs, and Corwin (1976) estimate that for an inclination of $59°$ the total mean internal extinction for M81 should be $A_B = 0.38$ mag (or $A_v = 0.3$ mag), which is significantly smaller than the values we measure for the giant H II regions.

b) Radial Distribution of Extinction in the Plane of M81

Figure 6 shows our values of $A_v(20)$ plotted as a function of galactocentric radius R. A graph of $A_v(6)$ versus R gives similar results. There is appreciable scatter in A_v at any given R, but over the range of R where we detect giant radio H II regions ($R = 4'$–$9'$), the radial distribution of extinction is fairly flat. Because of our measurement uncertainties, a gradient less than 0.1 mag kpc^{-1} would not be detected. From linear regressions

of $A_v(20)$ on R and $A_v(6)$ on R, we find that the slope of the regression line is less than the dispersion and that the correlation coefficient $|\rho| \le 0.39$ at both wavelengths. Thus, in the range $R = 4'$–$9'$, the relation between A_v and galactocentric distance shows no trend. Furthermore, it is clear from Figure 6 that the scatter in the values of A_v at fixed R is not just the result of measurement errors. Also, we find that some neighboring H II regions (e.g., sources 156 and 152; 172 and 173) differ appreciably in A_v. Thus, our data indicate that the dust distribution is patchy.

The absence of a radial extinction trend in M81 may be contrasted with Sarazin's (1976) results for the late-type spirals M101 and M33. On the basis of a small sample of H II regions, he finds significant radial extinction gradients in these two galaxies. Our data imply that not all spiral galaxies have appreciable extinction gradients over the range of R where the optical spiral arms are prominent. Sarazin (1976) suggests that internal extinction should increase with metal abundance. Stauffer and Bothun (1984) and Garnett and Shields (1986) have done spectrophotometry of some H II regions in M81. Over the range of radial distances treated here ($4'$–$9'$), the oxygen abundance values in these two papers imply a radial O/H gradient of about -0.07 dex kpc^{-1} and a mean oxygen abundance nearly solar. Despite the presence of this metallicity gradient, we see no extinction gradient. However, the results of Viallefond, Goss, and Allen (1982) imply that the comparison should be made between the dust-to-gas ratio and the metallicity rather than between the extinction and the metallicity. We note that if the gas column density and degree of clumpiness vary from region to region in M81, this could wash out any gradient in internal extinction that otherwise might have been present and thus explain our failure to detect a radial extinction gradient.
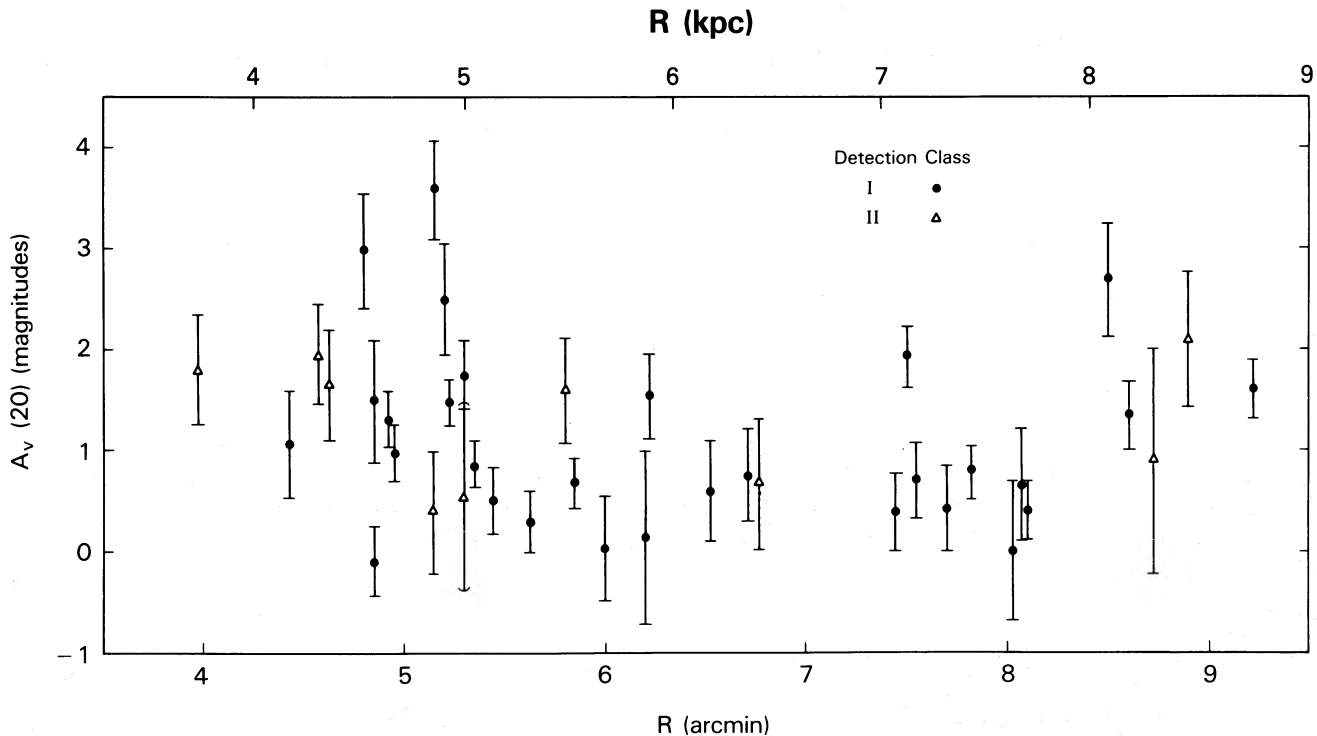

FIG. 6.—$A_v(20)$ as a function of galactocentric distance

Our list of giant radio H II regions has 13 H II regions in common with the set of optical H II regions measured by Garnett and Shields (1986). For these regions we find a mean $A_v(20) = 0.7 \pm 0.3$ mag [mean $A_v(6) = 0.6 \pm 0.4$ mag] if $T_e = 10^4$ K or a mean $A_v(20) = 0.9 \pm 0.3$ mag [mean $A_v(6) = 0.9 \pm 0.4$ mag] if we use the T_e values from Garnett and Shields. From the Balmer decrement, Garnett and Shields find a mean A_v(Balmer) of 0.4 mag if a standard reddening law is adopted. As their 4″ aperture is smaller than our 10″ resolution, this comparison provides borderline evidence for non-uniform extinction within the H II region. Recall that with nonuniform extinction the optical emission lines come preferentially from regions where the total optical depth is smaller.

Stauffer and Bothun find a much smaller mean reddening for their set of 10 H II regions than Garnett and Shields obtain for their set of 18 H II regions. (The list of H II regions observed by Stauffer and Bothun has only two regions in common with either the list of Garnett and Shields or with our list.) We suggest three possible explanations for the difference in mean reddening. (1) There is a real difference between the two samples: the distribution of extinction in M81 is patchy, and Stauffer and Bothun may have accidentally selected the H II regions with very little dust. (2) Since Stauffer and Bothun employed a 1″3 × 2″7 aperture, there may have been instrumental problems associated with the use of the smaller aperture. (3) If the distribution of reddening is nonuniform within the H II region, then centering the smaller of the two apertures on the brightest optical emission tends to select the area with less dust.

In Sarazin's model, most of the extinction comes from dust internal to the H II regions. However, this may not be the case in M81. While we have argued that most of the dust producing the 1 mag extinction is internal to M81, the agreement between the mean values of A_v for the giant radio H II regions and for the two M supergiants measured by Humphreys *et al.* (1986) suggests that much of this dust may, in fact, be external to the H II regions. This curious result needs to be checked with A_v measurements of a larger number of luminous stars in M81.

VI. DISTRIBUTION OF GIANT RADIO H II REGIONS IN THE PLANE OF M81

a) Azimuthal Distribution

Figure 7 shows the distribution of giant radio H II regions deprojected into the plane of M81. The east and west arms and part of the inner ring are clearly delineated in this plot. The spiral arms defined by the giant radio H II regions correspond well with the spiral arms in the lower resolution, face-on, 20 cm continuum map displayed in Figure 15 of Bash and Kaufman (1986). In the latter map the spiral arms are defined by the combination of nonthermal radio emission and the giant radio H II regions. Kaufman and Bash (1986) compare the distribution of giant radio H II regions with the VLA H I map of M81 made by Hine and Rots (1987); except for source 9 in Table 3, all the giant radio H II regions are located on either the inner H I ring or the broad H I arms.

Two compilations of optical H II regions in M81 have been published: Hodge and Kennicutt (1983*a*, *b*) list the coordinates of 801 H II regions and show the face-on distribution; CMT present a face-on plot of 349 H II regions. Neither of these papers distinguishes between bright and faint H II regions. The inner ring and the west arm are more clearly seen in the Hodge and Kennicutt plot than in the plot by CMT. However, neither of the optical sets is as closely confined to the spiral arms as the set of giant radio H II regions shown in Figure 7. Both face-on plots of the optical H II regions contain a greater number of interarm H II regions than one would predict if the set of giant radio H II regions were a random sample from the same distribution as the total set of optical H II regions. This is similar to the situation that Rumstay and Kaufman (1983) find in M83 and M33. They suggest that the stars in the low-luminosity H II regions are more likely to have formed as a result of stochastic processes. From the distribution shown in Figure 7, we conclude that in M81, also, the set of H II regions most closely related to the spiral arms (and thus most suitable for testing density wave theories) is the set of giant radio H II regions.
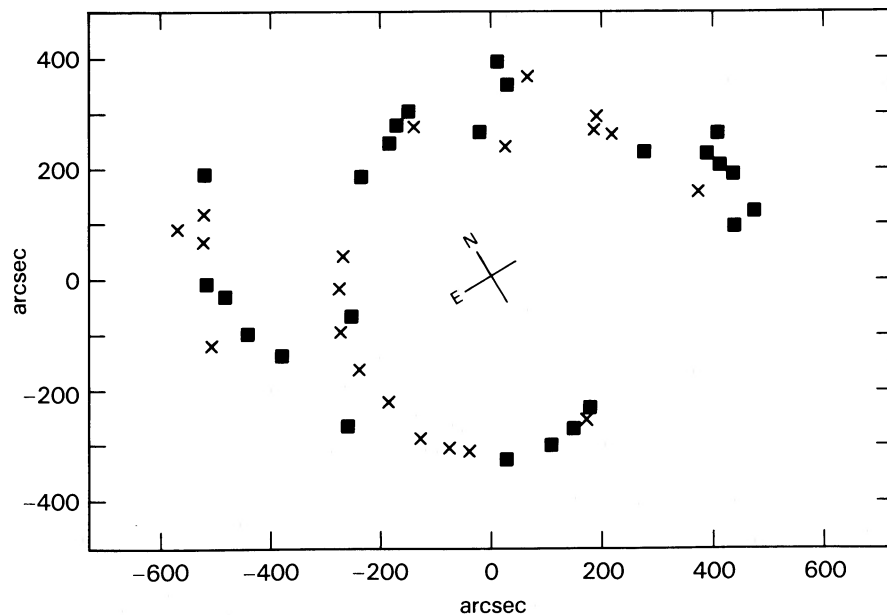

FIG. 7.—The distribution of giant radio H II regions in the plane of M81. The minor axis is horizontal. The solid squares represent H II regions with excitation parameter $U > 180$ pc cm^{-2}; the x's, those with $U = 130$–180 pc cm^{-2}.

b) Radial Distribution

Visser (1980b) and Leisawitz and Bash (1982) compare their models for star formation by a density wave with the radial distribution of optical H II regions from CMT. Figure 8 shows our radial distributions of giant radio H II regions and the radial distribution of optical H II regions given by CMT. In these plots, N(H II) is the relative number of H II regions per kpc^2, with the maximum normalized to 1. In the classification scheme of Hodge and Kennicutt (1983b), these radial distributions are characterized as ring-shaped, with a deep central minimum. The radial distribution of optical H II regions shown by Hodge and Kennicutt (1983b) for M81 is similar in morphology to the CMT distribution, but Hodge and Kennicutt used much broader bins. The radial distribution of giant radio H II regions exhibits a prominent ring at $R = 270''-350''$ ($R = 4.3-5.5$ kpc). Figure 8 shows the unweighted distribution of giant radio H II regions as well as one in which N(H II) is weighted by the net 20 cm flux. The most luminous regions occur in the range $290''-340''$. Aside from the maximum near $R = 300''$, the average 20 cm flux per giant radio H II region does not have much radial trend over the range $270''-570''$.

The spread of the radial distribution in the plane of a galaxy can be described by the rms scale s_R where

$$s_R{}^2 = (n-1)^{-1} \sum_{i=1}^{n} (R_i - \langle R \rangle)^2 , \qquad (4)$$

and $\langle R \rangle$ is the mean value of R. For the unweighted distribution of giant radio H II regions, $s_R = 1\rlap{.}'5$ (1.4 kpc). Rumstay and Kaufman (1983) compute values of s_R for the radial distributions of H II regions in M33 and M83 and find 1.4 kpc for the giant radio H II regions in M33 and 1.3 kpc for the giant optical H II regions in M83. The radial distribution in M33 is not ring-shaped. However, if the distances adopted from M81, M83, and M33 (i.e., 3.3 Mpc, 3.8 Mpc, and 0.72 Mpc, respectively) are correct, then the values of s_R for the set of high-luminosity H II regions are roughly the same in these three galaxies. This intriguing coincidence needs to be checked in a larger sample of spiral galaxies.

The exponential scale length R_0, defined so that $N \propto e^{-R/R_0}$, is often used to characterize a radial distribution in the disk of a spiral galaxy. In M81, the value of R_0 from the main peak (near 300'') outward is 1.6 ± 0.4 kpc for the unweighted distribution of giant radio H II regions and 1.8 ± 0.8 kpc for the flux-weighted distribution. Exponential decay gives a poor fit to the flux-weighted distribution. These values for R_0 are considerably less than the blue-light scale length of 3.0 kpc measured by Elmegreen and Elmegreen (1984) for the disk plus the arms and are, in fact, closer to their Johnson I-band scale length of 2.2 kpc. Thus the regions of intense O star formation that produce the H II regions detected in the radio are distributed differently as a function of galactocentric distance than
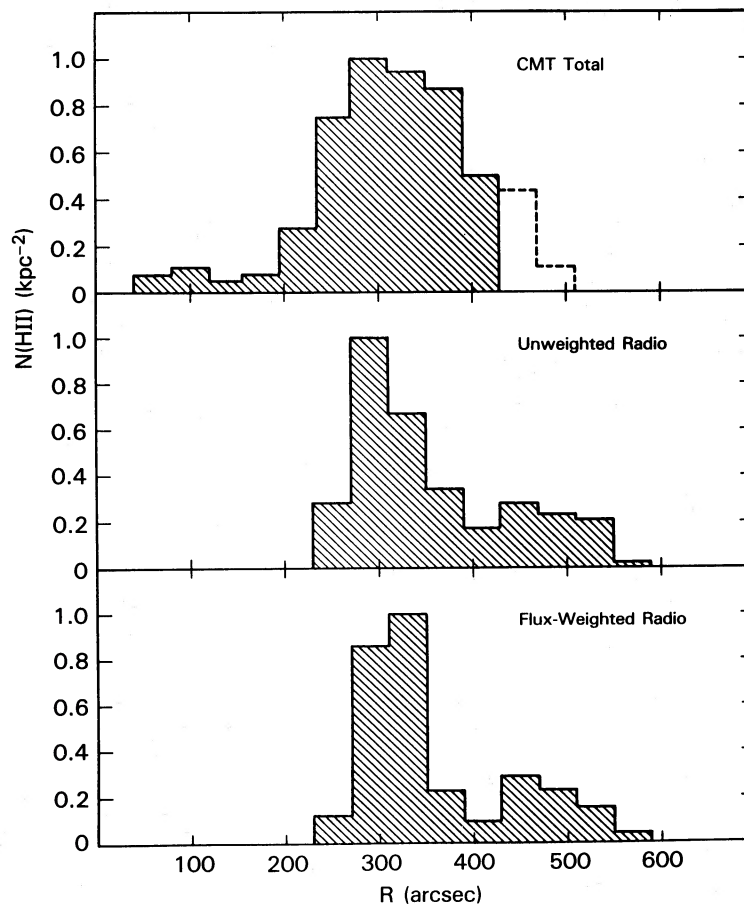

FIG. 8.—Comparison of the relative radial distributions of H II regions in the plane of M81. The radio distributions represent the giant radio H II regions in this paper. The "flux-weighted" distribution has been weighted by the 20 cm flux. The CMT distribution represents the total set of optical H II regions detected by CMT. For $R > 430''$, where CMT point out that their plate coverage is seriously incomplete, we represent their data by a dashed line.

the less luminous groups and later spectral types that produce most of the blue light.

We consider the flux-weighted distribution to be a better index of the distribution of O stars, despite the fact that the luminosity of an H II region is not a direct measure of the stellar ionizing flux (i.e., some Lyman continuum photons may be absorbed by dust). For 27 H II regions in our Galaxy, Rumstay (1986) concludes that the measured Hα and radio continuum luminosities of an H II region correlate with the stellar ionizing flux derived from model atmospheres and the known exciting stars. He finds that if one applies Strömgren theory to the radio continuum fluxes of his set of H II regions, then one underestimates the stellar ionizing flux by 30%–40% on the average. Although the galactic H II regions measured by Rumstay are less luminous than most of the giant radio H II regions in M81, we assume that the fluxes listed in Table 2 correlate with the stellar ionizing flux. We feel that the flux-weighted distribution of giant radio H II regions is the appropriate distribution for testing the star-formation rate predicted by density wave theories. As we shall see below, this can provide a quite stringent test.

Visser (1980*b*) and Leisawitz and Bash (1982) compare their density-wave predictions with the radial distribution of optical H II regions given by CMT. The CMT distribution includes faint H II regions as well as bright ones. The radial distribution of giant radio H II regions is clearly more sharply peaked than the CMT distribution. Therefore we need to reanalyze the models in light of these new data.

Visser (1980*b*) takes

$$N(\text{H II}) \sim \sigma_{\text{H I}}(\Omega - \Omega_p)(\sigma_{\text{max}}/\sigma_g)^j, \quad j = 1, 2, \qquad (5)$$

where $\sigma_{\text{H I}}$ is the mean surface density of H I at R, $\Omega(R)$ is the angular rotation speed, Ω_p is the pattern speed, and $\sigma_{\text{max}}/\sigma_g$ is the spiral shock compression. His model 3 with $j = 2$ produces a peak at $R = 300''$ and gives a reasonable fit to the CMT distribution. But none of the models plotted in his paper produces the very narrow peak that we find in the distribution of giant radio H II regions. One reasonable alternative is to replace $\sigma_{\text{H I}}$ in equation (5) by the surface density of atomic plus molecular hydrogen. If molecular hydrogen in M81 is concentrated at $R \approx 300''$, then one may get a better fit to our observations. However, at present the distribution of molecular hydrogen in M81 is unknown.

In the models of Leisawitz and Bash (1982, 1984), giant molecular clouds (GMCs) are formed at the spiral shock front, orbit as ballistic particles in a gravitational field perturbed by a spiral potential, and may collapse to produce stars after a time delay determined by collisions with small clouds. With GMC birth sites spaced uniformly in R along the spiral arms, they obtain a radial distribution of H II regions that fits the CMT distribution except that the theoretical maximum is located at $210''$–$250''$ while the observed value is $R \approx 300''$. Now, in discussing the H I ring, Bash and Kaufman (1986) suggest that the adopted location of the inner Lindblad resonance should be shifted outward by about $80''$. To first order, this also appears to be the shift necessary to get the theoretical and observed peaks in the distribution of H II regions to agree in position.

There are two ways in which the models of Leisawitz and Bash can be altered to produce the more narrow peak required to fit the observed distribution of giant radio H II regions: (1) assume that in M81 the GMC birth sites are concentrated near $R \approx 300''$; (2) change the adopted distribution of small clouds.

Alternative (1) can be tested by making high-resolution CO observations of M81. Leisawitz and Bash mention two examples of alternative (2); in fact, they rejected their models 3 and 5 because the resulting theoretical peak was too narrow to fit the CMT distribution. We suggest, in particular, that their model 5 should be reconsidered.

The plots in Figure 8 suggest that the set of high-luminosity H II regions is more sharply peaked in radial distribution than is the set of low-luminosity H II regions. One caution here is that the CMT data suffer from incomplete plate coverage that could seriously affect the radial distribution for $R > 430''$. From the north and south Hα plates described in § II, Kennicutt, Hodge, and Edgar (1987) have made a new tabulation of 513 optical H II regions with measured Hα fluxes. This listing does not have problems with incomplete plate coverage. The unweighted radial distribution of this new optical set, which includes both bright and faint H II regions, can be described as follows: (1) the location of the main maximum is near $R = 300''$, similar to the distribution shown in Figure 8; (2) the peak is broader than in the CMT distribution. This confirms that as a function of galactocentric radius the distribution of giant radio H II regions shows a more narrow maximum than the distribution of lower luminosity H II regions. Again this is similar to the situation that Rumstay and Kaufman find in M33 and M83, when they compare the distributions of high- and low-luminosity H II regions.

VII. CONCLUSIONS

The following are the main results of our Hα and radio continuum measurements of 42 giant H II regions with high surface brightness in M81.

1. The radial distribution of extinction along the spiral arms shows no trend. Over the range 4′–9′, the upper limit to the radial extinction gradient is 0.1 mag kpc^{-1}.

2. The mean value of 1.1 ± 0.4 mag for the visual extinction of the giant radio H II regions agrees with the values of A_v for the two M supergiants measured by Humphreys *et al.* (1986). This may indicate that for most of our sample, dust internal to the H II regions makes only a minor contribution. If this is the case, then our measurements pertain to the general extinction within the spiral arms. The absence of a radial gradient in extinction simplifies the interpretation of broad-band colors along the arms. On the other hand, the patchy character of the extinction affects distance estimates for M81 that depend on luminosity indicators: one needs to measure the extinction at the location of each luminosity indicator.

3. Nearly all of the giant radio H II regions lie along the spiral arms or the inner H I ring and, therefore, are suitable for testing density wave theories.

4. The radial distribution of giant radio H II regions exhibits a strong, narrow maximum at a galactocentric distance $R \approx 300''$ and is clearly more sharply peaked than the unweighted distributions of optical H II regions in CMT and Kennicutt, Hodge, and Edgar (1987), both of whom include faint H II regions as well as bright ones. Thus, M81 shows the same type of phenomenon that Rumstay and Kaufman (1983) find in the late-type spirals M33 and M83: the radial distribution of high-luminosity H II regions has a more narrow peak than that of low-luminosity H II regions.

5. If the assumed distances are correct, then the rms scale of the radial distribution of high luminosity H II regions is about the same in M81, M33, and M83, which are three spiral galaxies of rather different morphological types.

6. The observed radial distribution of giant radio H II regions disagrees with Visser's (1980b) simple model for the radial distribution of star formation associated with a density wave unless molecular hydrogen in M81 is concentrated near $R \approx 300''$. Therefore, it is important to look for CO in M81.

7. The ballistic particle model of Leisawitz and Bash (1982) needs to be reexamined in light of our new data since they constrained parameters to fit the CMT distribution which includes H II regions of low luminosity. To fit our data on the radial distribution of giant radio H II regions, their model requires (1) a shift in the position of the inner Lindblad resonance to approximately the location of the H I ring and (2) a different choice for the assumed radial distributions of either the GMC birth sites or the small clouds.

REFERENCES

Abolins, J., and Rice, W. L. 1986, *Star Formation in Galaxies Conference*, Pasadena, CA.
Arp, H. C. 1965, *Science*, **148**, 363.
Bash, F. N., and Kaufman, M. 1986, *Ap. J.*, **310**, 621.
Beck, R., Klein, U., and Krause, M. 1985, *Astr. Ap.*, **152**, 237.
Bottinelli, L., Gouguenheim, L., Paturel, G., and de Vaucouleurs, G. 1984, *Astr. Ap. Suppl.*, **56**, 381.
Boulanger, F. 1986, private communication.
Bruzual, A. G., Peimbert, M., and Torres-Peimbert, S. 1982, *Ap. J.*, **260**, 495.
Burstein, D., and Heiles, C. 1984, *Ap. J. Suppl.*, **54**, 33.
Chu, Y-H., and Kennicutt, R. C. 1986, *Ap. J.*, **311**, 85.
Connolly, L. P., Mantarakis, P. Z., and Thompson, L. A. 1972, *Pub. A. S. P.*, **84**, 61 (CMT).
de Vaucouleurs, G., de Vaucouleurs, A., and Corwin, H. S., Jr. 1976, *Second Reference Catalogue of Bright Galaxies* (Austin: University of Texas Press).
Elmegreen, D. M., and Elmegreen, B. G. 1983, *Ap. J. Suppl.*, **54**, 127.
Fomalont, E. B. 1982, in *Synthesis Mapping, Proceedings of the NRAO-VLA Workshop*, ed. A. R. Thompson and L. R. D'Addario (Greenbank, W. VA: NRAO), p. 11–1.
Garnett, D. R., and Shields, G. A. 1986, *Ap. J.*, in press.
Gebel, W. L. 1968, *Ap. J.*, **153**, 743.
Georgelin, Y. M., and Georgelin, Y. P. 1976, *Astr. Ap.*, **49**, 57.
Hine, B., and Rots, A. H. 1987, in preparation.
Hodge, P. W. 1986, in *IAU Symposium 116, Luminous Stars and Associations in Galaxies*, ed. C. de Loore, A. Willis, and P. Laskarides (Dordrecht: Reidel), p. 369.
Hodge, P. W., and Kennicutt, R. C. 1983a, *Ap. J.*, **88**, 296.
———. 1983b, *Ap. J.*, **267**, 563.
Holmberg, E. 1958, *Medd. Lunds Ap. Obs.*, Ser 2, No. 136.
Humphreys, R. M., Aaronson, M., Lebofsky, M., McAlary, C. W., Strom, S. E., and Capps, R. W. 1986, *A.J.*, **91**, 808.

Israel, F. P. 1980, *Astr. Ap.*, **90**, 246.
Kaufman, M., and Bash, F. N. 1986, *Star Formation in Galaxies Conference*, Pasadena, CA.
Kaufman, M., Kennicutt, R. C., and Bash, F. N. 1986, in *IAU Symposium 116, Luminous Stars and Associations in Galaxies*, ed. C. de Loore, A Willis, and P. Laskarides (Dordrecht: Reidel), p. 503.
Kennicutt, R. C. 1981, *Ap. J.*, **247**, 9.
Kennicutt, R. C., and Hodge, P. W. 1980, *Ap. J.*, **241**, 573.
———. 1986, *Ap. J.*, **306**, 130.
Kennicutt, R. C., Hodge, P. W., and Edgar, R. J. 1987, in preparation.
Leisawitz, D., and Bash, F. N. 1982, *Ap. J.*, **259**, 133.
———. 1984, *Ap. J.*, **285**, 25.
Magnani, L., and de Vries, C. P. 1986, preprint.
Mezger, P. G. 1970, in *IAU Symposium 38, The Spiral Structure of Our Galaxy*, ed. W. Becker and G. Contopoulos (Dordrecht: Reidel), p. 107.
Miller, J. S., and Mathews, W. G. 1972, *Ap. J.*, **172**, 593.
Peimbert, M., and Torres-Peimbert, S. 1981, *Ap. J.*, **245**, 845.
Rots, A. H. 1975, *Astr. Ap.*, **45**, 43.
Rumstay, K. S. 1986, *Ap. J.*, preprint.
Rumstay, K. S., and Kaufman, M. 1983, *Ap. J.*, **274**, 611.
Sandage, A. 1961, *The Hubble Atlas of Galaxies* (Washington, D.C.: Carnegie Institute).
Sarazin, C. L. 1976, *Ap. J.*, **208**, 323.
Shu, F. H. 1974, in *The Interstellar Medium*, ed. K. Pinkau (Dordrecht: Reidel), p. 219.
Stauffer, J. R., and Bothun, G. D. 1984, *A.J.*, **89**, 1702.
van der Hulst, J. M., Kennicutt, R. C., and Crane, P. C. 1987, preprint.
Viallefond, F., and Goss, W. M., 1986, *Astr. Ap.*, **154**, 357.
Viallefond, F., Goss, W. M., and Allen, R. J. 1982, *Astr. Ap.*, **115**, 373.
Visser, H. C. D. 1980a, *Astr. Ap.*, **88**, 149.
———. 1980b, *Astr. Ap.*, **88**, 159.

FRANK N. BASH: Department of Astronomy, The University of Texas at Austin, Austin, TX   78712

MICHELE KAUFMAN: Department of Physics, The Ohio State University, 174 West 18th Avenue, Columbus, OH   43210

R. C. KENNICUTT, JR: Department of Astronomy, University of Minnesota, Minneapolis, MN   55455

P. W. HODGE: Astronomy Department, FM-20, University of Washington, Seattle, WA   98195